CIMAC CONGRESS 25
ZURICH, MAY 19 – 23, 2025

2025 | 037

Approach for high methanol substitution by energy with conventional and bio pilot fuels

Fuels - Alternative & New Fuels

Derek Splitter, Oak Ridge National Laboratory

James Szybist, Oak Ridge National Laboratory
Gurneesh Jatana, Oak Ridge National Laboratory
Kenth Svensson, Caterpillar Inc.
Dave Montgomery, Caterpillar Inc.

ABSTRACT

Methanol is emerging as a promising alternative fuel for the commercial marine industry. However, methanol is not a drop-in fuel in the compression ignition engines that dominate the marine industry because it is difficult to ignite due to its low cetane number and high latent heat of vaporization. The most straight-forward way to use methanol in the compression ignition engines is to premix the methanol, such as with port fuel injection during the intake stroke, and ignite it with a diesel pilot injection. Because diesel fuel is still used in this strategy, it does not fully displace the petroleum diesel fuel. To completely displace the petroleum-derived diesel fuel, this investigation presents experimental results comparing diesel and biodiesel pilot ignition in a dual-fuel strategy with methanol in a marine-variant of a Cat® C18 18 L engine with a 145mm bore. Engine performance and emissions characteristics are presented that include effects of diesel vs. biodiesel across a series of fuel injection timing and other operating parameters, including intake manifold pressure and engine load. Results presented include in-cylinder pressure and combustion-related findings about heat release, methanol fuel energy substitution rates greater than 75% from 1 to 18 bar BMEP on a single cylinder engine at 1800 RPM. Criteria pollutants including particulate matter, NOx (NO and NO2), unburned fuel, and formaldehyde, as well as the overall BSFC and FSN of the combustion process relative to the baseline diesel operation.

1 INTRODUCTION

In recent years there has been increased interest in methanol as a marine fuel [1, 2]. A major motivator for this fuel transition is the potential for rapid decarbonization and fuel source diversification used in marine environment and shipping [3, 4]. An additional attractive aspect of methanol in these sectors is the potential for reduced environmental impact when spilled into aquatic environments. Specifically, methanol has been suggested to have a fast degradation rate and only local aquatic life environmental impacts as compared to conventional fuels [5]. Lastly there are over 120 ports worldwide bunkering methanol [6], making the ready availability of methanol at ports an attractive aspect to deploy an alternative fuel. These combined aspects motivate the development of methanol capable engines for marine use.

For primary power and/or auxiliary power engines in coastal and inland operations (i.e., not crosshead design 2-stroke engines), methanol fueled marine engines may require a dual fuel approach. Work on methanol dual-fuel retrofit compression-ignition engines has shown that combustion performance can be highly linked to intake temperature due to incomplete combustion and ignition issues for direct-injected fuels [7,8]. Thus, there is motivation to understand methods to improve combustion efficiency and to counteract the high enthalpy of vaporization of methanol [9], which is approximately 6 times that of diesel fuel on an energy-equivalent basis.

Retrofits [10] and multiple methanol port fuel injection strategies have been shown in a multi-cylinder engine (MCE) to offer methanol substitutions by energy approaching 80% at loads up to 10.5 bar brake mean effective pressure (BMEP) at 2000 revolutions per minute (rpm), and slightly lower methanol substitutions up to 12.5 bar BMEP at 1500 rpm, with a full load of the production engine of 15.9 bar BMEP at 1500 rpm and 14.2 bar BMEP at 2300 rpm. Recent simulation-based work on a large-bore marine engine has suggested that port injection of methanol could be a limiting factor for high methanol substitution ratios, and that direct injection of methanol could offer improved methanol substitution ratios [11]. Similar work by [12] showed that significant soot emissions were possible with methanol, but only demonstrated up to 40% methanol substitution by energy at 1800 rpm and 50% rated load.

Biomass-produced renewable methanol has been suggested as a potential marine fuel [13]. And e-methanol has recently been proposed as a method of storing hydrogen produced through electrolysis from renewably powered electricity [14, 15] and other associated methods [16, 17, 18]. Additionally, fossil-based methanol production can be paired with carbon capture and sequestration to produce blue methanol. For these three methods combined, there are currently planned plants for 37.5 million metric tons of production annually by 2030, which is equivalent to more than 1/3 of total 2024 methanol production [19].

Although methanol offers the potential to be a renewable fuel for maritime use, the reliance on diesel fuel in retrofit applications continues to insert a reliance on conventional fossil fuels. One additional pathway to reduce the reliance on fossil fuels in dual fuel engines is to use biodiesel as the pilot fuel in place of diesel fuel. Biodiesel is a diesel-like fuel made primarily from vegetable fats [20]. Recent interest in biofuels for the marine sector has also emerged [21], where reduced energy and refining into upgrading of bio-oils offers potential low-cost, attractive solutions to marine shipping. However, unlike these more residual-like fuels, biodiesel has physical and chemical properties more like those of conventional diesel fuel. Historically, a barrier to neat biodiesel use in maritime environments has been a limitation on biodiesel content being 7% in marine distillate fuels [22]; however, a recent modification in 2024 to accommodate a higher volume of biodiesel [23] has superseded the prior standard. Although not yet fully defined, the limit on biodiesel as a marine fuel is thought to increase and some of the consideration to its final implementation are captured by [24]. In this decision process much of the information and history of biodiesel in the on-

road space is being considered and adapted/modified to marine environments.

Interestingly, a similar parallel to prior on-road work can be made with methanol. Unlike the recent marine interest in methanol in compression ignition engines, use of methanol as a turbulent premixed fuel in spark ignition engines has been investigated for decades [25], including the development of methanol fuel specifications [26]. In fact, recent work in methanol turbulent premixed charge flame propagation engines has reemerged as a potential opportunity due to the beneficial fuel properties for spark ignition engines, such as high latent heat of vaporization and high-octane number [27,28,29,30].

The current work expands on prior efforts to increase methanol substitution and to introduce B100 as a pilot fuel for marine applications in a mixing-controlled compression ignition (MCCI) base engine. Although the approach uses a conventional MCCI marine base engine, the combustion approach is not relegated to only mixing-controlled processes. Work to explore expanding the opportunity of leveraging the high-octane number and high charge cooling of methanol in conjunction with ultra-low sulfur diesel (ULSD) or biodiesel (B100) as the pilot fuel in a dual fuel methanol approach. The B100 methanol approach offers the potential for a completely renewable fuel option.

2 EXPERIMENTAL SETUP

2.1 Engine, laboratory, and data acquisition

The experimental engine for this work was a purpose-built single cylinder engine (SCE) based on a Cat C18 combustion chamber geometry on a Southwest Research Institute-designed bespoke SCE crankcase. The SCE geometry is presented in Table 1 For all experiments, oil and coolant temperatures were maintained at 80 and 84°C, respectively. Engine load was absorbed by an AVL 450 kW AC dyno (ATV 400/560) operated in constant speed mode at 1800 rpm.

Table 1. Engine geometry

Parameter (units)	Value
Displacement Volume (L)	3.0
Bore (m)	0.145
Stroke (m)	0.183
Connecting rod length (m)	0.2708
Pin offset (m)	0
Geometric Compression ratio (-)	16.5:1
Number of cylinders (-)	1

Direct injection fueling for diesel and biodiesel was achieved using a Caterpillar common rail injector, fueled by a standalone common rail high pressure pump cart. This cart (Re-Sol RS905DE1) featured an electrical motor-driven Denso HP6 high-pressure pump which fed high pressure fuel into a diesel common rail (John Deere RE549624). The strategy to operate the pump to control rail pressure was devised as per data published from Denso [31]. The control commands to the HP6 pump need to be synchronized with the shaft position of the pump. Therefore, an optical encoder was mounted on the electrical motor to track pump position, and a National Instruments-based real-time controller was used to control the valves on the HP6 pump to achieve the desired rail pressure.

In this work, the MCCI data were acquired with a single direct injection (DI) strategy at 1600 bar rail pressure. The dual-fuel data acquired with a double DI strategy had the first start of injection (SOI) timing between -35 and -20°CA after top dead center firing ($aTDC_f$) with approximately a 10°CA dwell between the first and second injection SOI timings. The associated DI durations were varied between approximately 60/40 and 40/60 dwell splits between the first and second injections respectively. With the strategy the DI rail pressure was modulated between 500 bar and 1300 bar depending on the load. The adjustment of rail pressure resulted in similar DI timings and durations which were near the lower limit of duration for the fuel injection system.

The cylinder head had port fuel injection (PFI) injectors added in two locations: above the intake valves and at the interface between the cylinder head and the intake manifold. For all work presented herein, the port fuel injection location is the location at the cylinder head-intake manifold interface, which is further from the intake valves. The PFI injectors used are rated at 158 kg/hr flow rate (~3500 cc/min) and were a bespoke design (Billet Atomizer Fury 350). Fuel pressure was controlled by a boost-referenced rising rate fuel pressure regulator (Aeromotive 13132), with a base fuel pressure of 580 kPa and a rising 1:1 boost referenced to the intake manifold. Methanol was supplied via a lift pump (Tuthill TXS5.3EEET3NNF1000) at 1725 rpm powered by a 0.5 HP electric motor. Methanol was stored in a stainless-steel fuel tank. All fuel lines for the methanol fuel supply were stainless steel or PTFE lines, and fuel was filtered by an injector dynamics filter (IDF1250) rated for methanol.

Engine control and data acquisition were conducted by a National Instruments based controller with an ORNL-developed combustion analysis program, Oak Ridge Combustion Analysis System, which follows common accepted practices for combustion analysis and heat release

calculation [31]. In-cylinder pressure was measured by an AVL pressure transducer (AVLGH14D), with an integrated torque transducer for brake measurements, and engine speed was acquired by an AVL encoder (365C01) with a crank resolution of 0.2°CA. Note, all brake emissions and efficiency measurements reported are calculated directly from the dynamometer torque readings on the SCE and not obtained from a correlation from an MCE.

Airflow was supplied by an external air compressor (Ingersoll Rand RS55I), with an integrated air dryer resulting in relative humidity of the supplied air of less than 20% at 20°C. Air from the compressor to the engine was controlled by two Alicat mass flow controllers used in parallel (Alicat 5000SLPM and 2000SLPM). The air was thermally conditioned using a 6 kW heater (Tutco SureHeat Max F074726) to a constant temperature of 40°C in the intake runner upstream of the methanol port fuel injection locations for all experiments.

Intake and exhaust surge tanks of 100 L volume, 33 times more than the geometric displacement of the engine, were mounted within 1 meter of the engine. After the exhaust surge tank, a backpressure controller (Flowserve MK330S) enabled simulated turbocharging, where for much of the dual fuel experiments the exhaust pressure was slightly higher than the intake pressure.

Exhaust emissions were simultaneously measured after the backpressure controller by a conventional 5-gas emissions bench (California Analytical Instruments 700 series instruments) and an FTIR (MKS Multigas). The FTIR used a method specifically developed for methanol, resolving up to 10,000 ppm methanol concentration levels. Soot emissions were measured by an AVL 415S with paper save mode off and a sample size of 1, with a sample time of 6 seconds and a sample volume of 1 L. All recorded data were acquired with 500 consecutive cycles recorded at each condition.

2.2 Fuels

The PFI methanol fuel properties are presented in Table *2*, and the DI fuel properties are presented in Table 3.

Table 2. Critical methanol fuel properties

Property (unit)	Value
Density (kg/m^3)	791
Heating value (mJ/kg)	19.9
Hydrogen/carbon ratio (-)	4
Oxygen/carbon ratio (-)	1
Research octane number (-)	108.7 [33]
Motor octane number (-)	88.6 [33]

Table 3. Critical direct injection fuel properties

Property (unit)	ULSD	B100
Density (kg/m^3)	839.7	833.13
Kinematic viscosity (mm^2/s)	2.528	4.046
Heating value (mJ/kg)	42.901	37.309
Hydrogen/carbon ratio (-)	1.8192	1.8580
Oxygen/carbon ratio (-)	0	0.1076
Nitrogen/carbon ratio (-)	0	0
Derived cetane number (-)	43	47.5

3 RESULTS

The results of this work are presented in 4 subsections. The sections describe the operating strategy developed to employ high (>75%) methanol substitution by energy from idle to high load, describe and quantify the operational strategy with ULSD and B100 as the DI fuel, describe the operational performance and emissions with ULSD and B100 as the DI fuel, and lastly highlight emissions observations between ULSD and B100 methanol dual fuel and MCCI. Throughout the subsections the self-imposed operating constraints in Table 4 were employed for both ULSD and B100 methanol dual fuel operation.

Table 4. Imposed operating constraints

Constraint	ULSD
CoV $IMEP_n$	< 5
NOx (g/kW-hr)	< 9
$\eta_{combustion}$ (%)	≥ 90
MPRR (bar/CA)	< 10 for +99% of cycles
FSN (-)	< 1
$BSFC_{SCE}$ $ULSD_{eq}$ (g/kW-hr)	≤ ULSD MCCI
CH_3OH substitution (% energy)	≥ 75

3.1 Dual-fuel operating strategy for high methanol substitution

The dual-fuel operating strategy described in this manuscript was developed to maximize methanol substitution over a wide load space within the constraints of Table 4. Figure 1 illustrates the methanol substitution as a function of load and combustion phasing at 1800 RPM operating speed. The results indicate that high levels of methanol substitution by energy are possible in a marine-relevant heavy duty four-stroke engine. Increasing methanol substitution is possible with increasing load, which is a synergistic relation for the opportunity to maximize petroleum displacement and decarbonization potential with green methanol. Methanol energy fraction in Figure 1 was calculated by multiplying the measured mass flow rate of

methanol by the ratio of the lower heating values of methanol to the DI fuel (i.e., not a mass ratio).

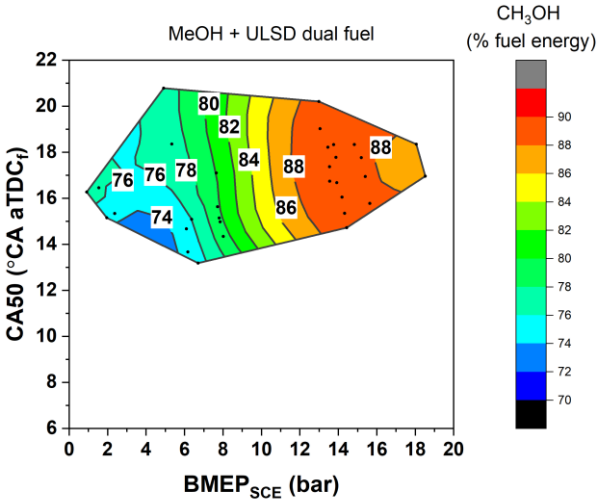

Figure 1. Map of methanol substitution possible with respect to load and combustion phasing at 1800 rpm. Results show that over 75% methanol substitution was possible for all loads.

To achieve the operational space with high levels of methanol substitution, it was necessary to alter the levels of boost, backpressure, and DI timing from conventional MCCI operation. The first aspect of this approach, boost, is addressed relative to MCCI in Figure 2, where clearly MCCI is much more dilute than the dual fuel approach used, ~25% more air is needed in MCCI. The additional air in MCCI is used to help lean the local equivalence ratios within the highly heterogeneous diffusion flame and mixing process used in MCCI. The additional air not only reduces soot (e.g., filter smoke number (FSN)) but also enables load expansion. However, Figure 3B depicts that the dual fuel strategy with methanol has much lower FSN than single direct injection ULSD MCCI does (Figure 3A). Note that this low FSN is also occurring with ~25% less air than MCCI requires. Thus, the need for high levels of boost is not required as long as the methanol substitution level is high (Figure 1).

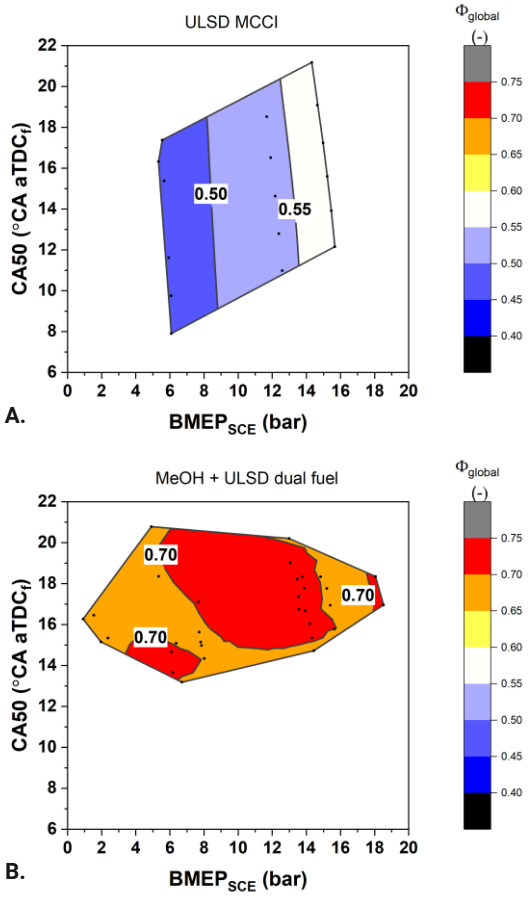

Figure 2. Maps of global equivalence ratio (Φ) for MCCI (A) and ULSD methanol dual fuel operation (B), plotted with respect to load and combustion phasing.

The effect of reduced boost on brake specific fuel consumption (BSFC) and the associated operating input parameters are depicted in Figure 4, where the combustion control input parameters and BSFC are plotted as a function of intake pressure at a constant 50% mass fraction burned (CA50) load and methanol substitution level. There is a trend of reduced BSFC with reduced boost. Also observed is that as boost is reduced the direct injection timing advances, and the backpressure changes. Note that the backpressure is not changing at a one-to-one level with boost, and that increasing backpressure is actually being applied as boost is reduced. This relation was quantified as the term ΔP, in Equation 1.

$$\Delta P = P_{exhaust} - P_{intake} \quad (1)$$

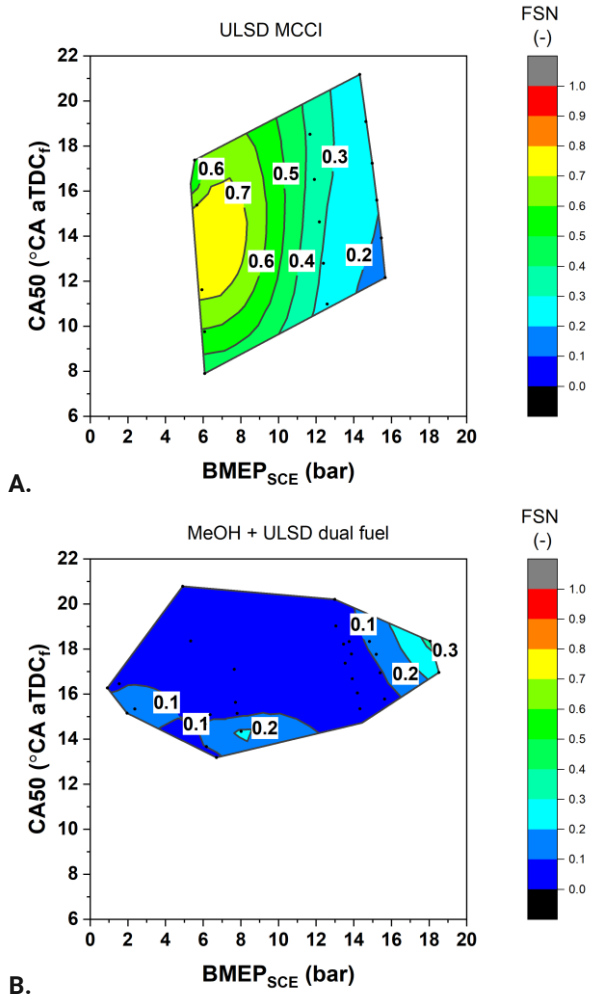

Figure 3. Maps of FSN for MCCI (A) and ULSD methanol dual fuel operation (B), plotted with respect to load and combustion phasing.

Likewise because there was constant fueling used in the results of Figure 4, the premixed equivalence ratio ($\phi_{premixed}$) of methanol is also increasing, where $\phi_{premixed}$ is defined in Equation 2.

$$\phi_{premixed} = \frac{\frac{air}{fuel}_{stoichometric}}{\frac{air}{fuel}_{actual}} \qquad (2)$$

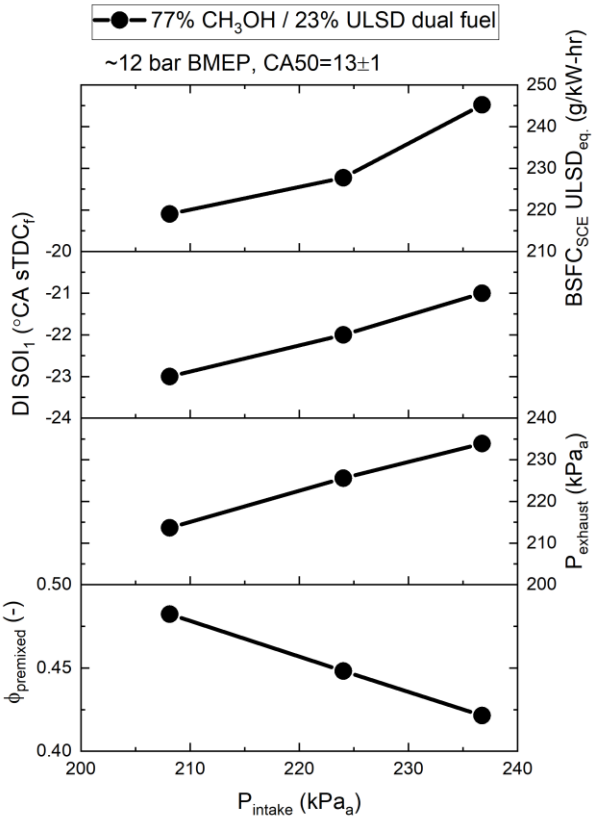

Figure 4. Trends in premixed equivalence ratio (bottom), backpressure (second from bottom), fuel injection timing (second from top), and ULSD-normalized BSFC (top) with respect to intake pressure at constant load and combustion phasing and methanol substitution level.

The goal of this work is to maximize methanol substitution over the widest load range possible while remaining within the constraints of Table 4. Results in Figure 4 highlight that three are interdependencies of several variables that affect performance, where appropriate relations were gleaned from these interdependencies to enable high methanol substitution rates with low fuel consumption. Specifically, increasing Δp can be a control mechanism by increasing hot trapped residuals in-cylinder. Empirically increasing Δp was found to offer appropriate control authority to enable high levels of methanol substitution of all the control parameters investigated in this study. Recent work by others has also suggested similar control opportunities through increasing hot trapped residuals with alcohol fuels used in compression ignition engines [34]. Note that although not shown, at high methanol substitution ratios and low λ_{global} the $\gamma_{compression}$ (ratio of specific heats of the compression working fluid) decreases relative to 0% EGR MCCI operation from both composition and charge cooling. The result of the $\gamma_{compression}$ combined with the high enthalpy of vaporization (HoV) of methanol is that the

compression temperature at the time of diesel injections is greatly reduced, which can cause misfire and poor performance.

To illustrate the thermodynamic relations of premixed methanol its HoV compared to MCCI, Figure 5 plots contours of the theoretical in-cylinder temperature for the engine in this study at -40°CA aTDC$_f$ (i.e. the in-cylinder temperature near the timing of the first direct injection timing). The contours are presented as a function of temperature at intake valve closing (x-axis) and $\gamma_{compression}$. (y-axis). The approach to calculate the variables in Figure 5 employs well documented polytropic gas relations [32], using gas property relations from [35]. The data points are corresponding output from fundamental thermodynamic calculations exploring different thermodynamic effects, each effect is applied to initial conditions (i.e. air fuel ratio, exhaust temperature, trapped residuals, etc.) from the measurements in this work. The corresponding output data of the simulation are color coded, highlighting the thermodynamic effect considered in methanol dual fuel.

As shown, adding premixed methanol—the green data presented in Figure 5—reduces $\gamma_{compression}$ compared to MCCI. Additionally, there is a small reduction in T_{IVC} also, which results from the methanol reducing the heating effect that trapped residuals have (only 5% trapped residuals here). Note, HoV is ignored in this portion of the assumptions, and only composition effects are determined. The result of lower $\gamma_{compression}$ and T_{IVC} is that the temperature at -40°CA aTDC$_f$ (contour line) is approximately 50 K lower than that of MCCI. This result and assumption of no HoV effect is like that which would occur if methane were used for dual fuel instead of methanol.

However, unlike methane and other more common premixed fuels used in dual fuel engines, methanol has a substantial HoV, 37.34 kJ/mol used herein. Accounting for the HoV results in moving from the green data to the blue data. Note, this calculation assumes that all of the charge cooling happens instantaneously at intake valve close. The result of calculated cooling is that T_{IVC} reduces by around 100 K, and $\gamma_{compression}$ increases, a result of the reduced temperature from HoV. Note that the resulting temperature at -40°CA aTDC$_f$ is now approximately 150–200 K cooler than MCCI, resulting in poor ignition of direct-injected diesel fuel.

To combat the effect of charge cooling, increased backpressure can be used, resulting in moving from the blue data to the purple data. Backpressure increases trapped residuals, which helps to offset HoV. Although backpressure does reduce $\gamma_{compression}$ from composition changes, the effect is small. The total result is that methanol HoV can be counteracted, and the resulting T_{IVC} and $\gamma_{compression}$ can remain relatively unchanged from that of only the effect of gamma. Note that the purple data series in Figure 5 shows the actual data recorded and moves from right to left as load increases, i.e. more backpressure was needed at lower loads). Also note that the relations in Figure 5 are from the present work with 75–90% premixed methanol by energy; if the methanol levels were reduced or increased the trends would move closer or further away from MCCI respectively.).

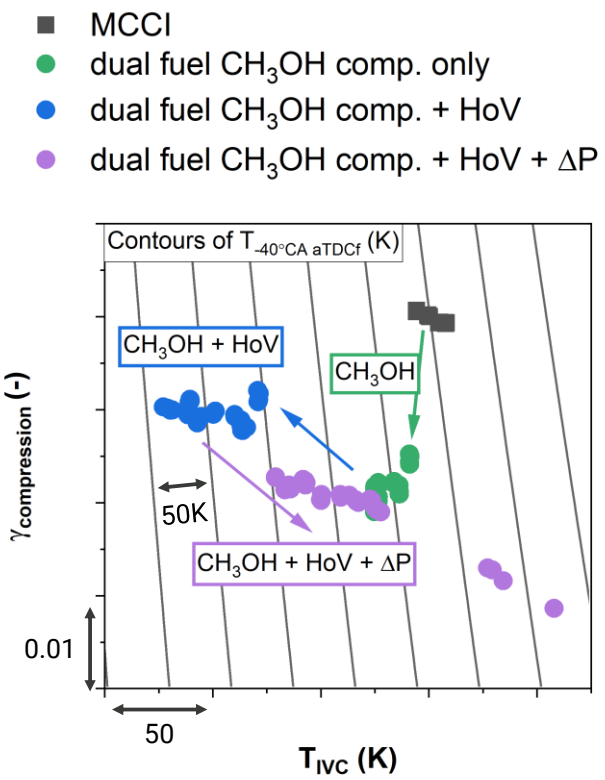

Figure 5. Modeled contours of in-cylinder temperature at 40 crank angles before top dead center (TDC) (around the first DI timing used in this work) as a function of intake valve closing temperature and polytropic compression exponent. Markers are thermodynamic modeled results based on experimental data inputs from this study for MCCI (squares) and dual fuel (circles) shaded as a function thermodynamic effect considered.

3.2 Operational strategy and load-combustion phasing authority with ULSD and B100 as the DI fuels

3.2.1 ULSD methanol dual fuel controllability

The cylinder pressure, AHRR, and direct injection current command traces with ULSD are presented in Figure 6. The mean cylinder pressure values are calculated from unfiltered pressure (i.e., raw

measured pressure). Analysing the data in this manner reveals additional detail about the combustion behavior of the load sweep.

The data in Figure 6 show that as a function of load, there is combustion regime evolution. Note that prior work by others has highlighted that multiple combustion regimes, including mixing and kinetically dominated processes, can exist in methanol/diesel dual fuel engines with regimes resulting from charge preparation and injection strategy differences [36]. In the present work, there is evidence of combustion regime differences, but the findings are more consistent with those of transitioning from mixing to turbulent premixed combustion rather than transitioning from mixing to kinetically controlled combustion regimes.

Figure 6 highlights that at the lowest loads there is evidence of premixed spike followed by what appears to be diffusional or turbulent premixed combustion processes in the cylinder pressure and AHRR. This multi-mode process occurs despite having quite advanced double direct injection timings at these loads. The advanced injection timings are used in conjunction with high trapped residuals to combat the charge cooling of the high methanol substitution rate (>~75%). The combined effect of these factors results in a balancing of the ignition delay of the methanol/ULSD mixture accordingly. The resulting bimodal AHRR combustion behavior suggests the presence of an initial bulk premixed burn followed by a slower mixing and or premixed flame process.

However, as load increases to ~8 bar BMEP the cylinder pressure and corresponding AHRR evolve from the multi-mode process to more uniformly progressing combustion, emulating premixed flame propagation, like that of a premixed turbulent flame (i.e., spark-ignition-like) combustion process.

This premixed propagating reaction combustion regime is maintained through the load sweep. As load increases, combustion is phased later. At these higher loads, the methanol substitution rate is nearly 90% for all conditions. Likewise, the combustion phasing is relatively constant, and the highest load was over 20 bar net indicating mean effective pressure ($IMEP_n$) with exceptional performance (Figure 11, Figure 12) and controllability.

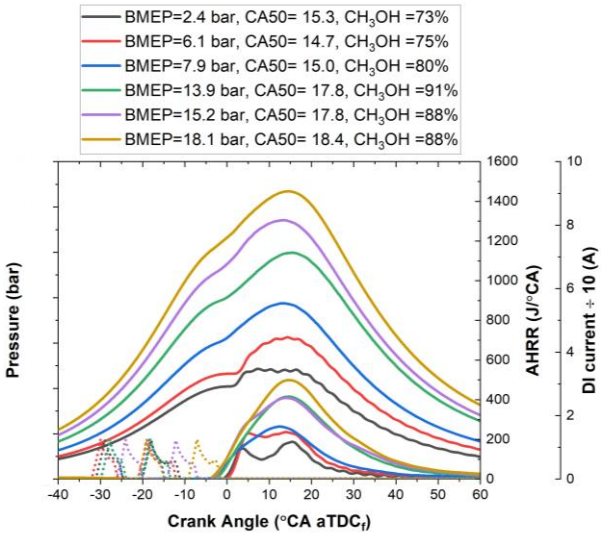

Figure 6. Mean values of indicated cylinder pressure, AHRR, and direct injection current commands.

To illustrate the linearity of injection timing in both MCCI and dual fuel the combustion phasing change as a function of SOI timing are shown in Figure 7.

Results of Figure 7 depict that the dual fuel approach behaves like MCCI or spark ignition, in that advancing injection timing (e.g., spark timing in SI combustion) also advances combustion phasing. Regardless, Figure *7* proves that 89% fuel energy methanol/11% fuel energy ULSD dual fuel operation at the equivalent of ~1700 Nm torque in a multi-cylinder C18 engine has high control authority from traditional MCCI input parameters.

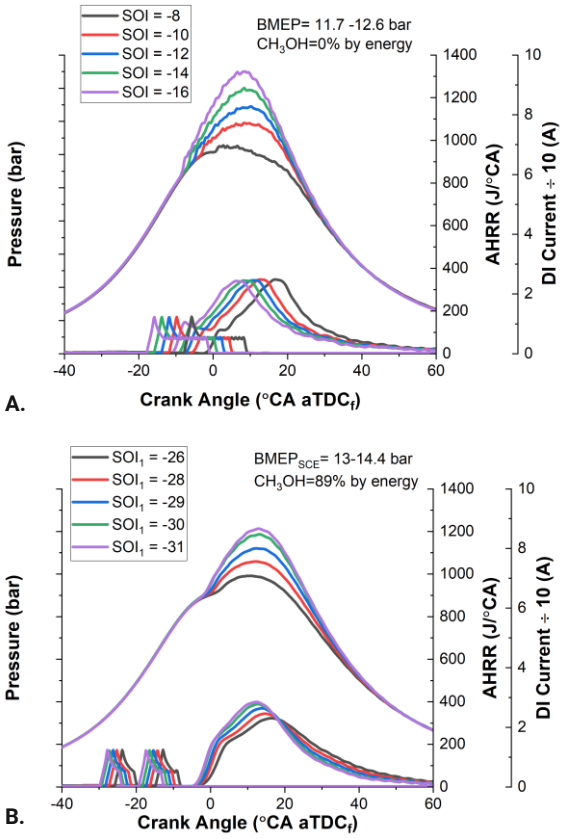

Figure 7. A. ULSD MCCI SOI sweep, B. 89% by energy methanol balance ULSD SOI sweep. Both strategies are at approximately Mode 3 operating condition.

Figure 8 quantifies these results where both MCCI and the dual fuel approach exhibit a high one-to-one CA50 to SOI relationship. The combustion control input to output quantification scheme employed in Figure 8 is a difference method, described in Equations 4 and 5, where the $CA50_1$ is the initial (i.e., most advanced) CA50, and $CA50_n$ is a given CA50 in the sweep of Figure 7. Likewise, SOI_1 is the initial (i.e., most advanced) SOI, and SOI_n is a given SOI in the sweep of Figure 7. For the methanol dual fuel, the first SOI timings were used, and for MCCI the main SOI (the only SOI) timings were used in Equation 5.

$$\Delta CA50 = CA50_n - CA50_1 \quad (4)$$

$$\Delta \mathrm{SOI} = SOI_n - SOI_1 \quad (5)$$

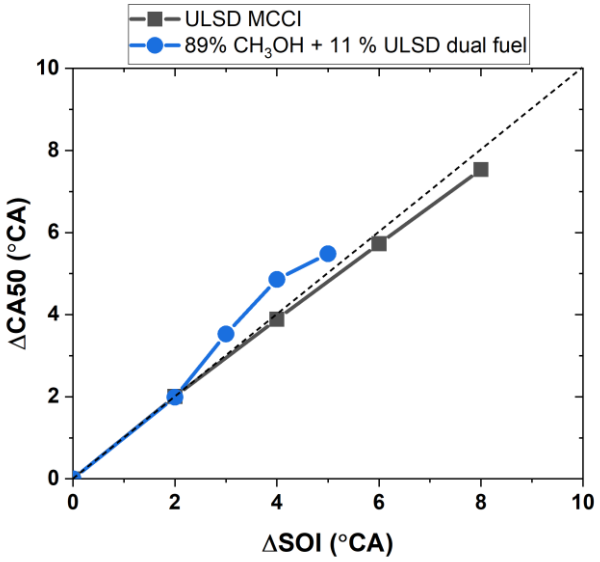

Figure 8. Direct Injection timing control authority on combustion phasing for MCCI and 89% methanol by energy dual fuel for the data in Figure 7B.

Figure 9 highlights that as combustion is advanced (Figure 9B), knock is encountered. If combustion is retarded, through retarding of the injection timing, knock can be mitigated (Figure 9A). The quantified maximum pressure rise rate (MPRR) is shown in Figure 9C, where excursions above the 10 bar/°CA account for less than 1% of the cycles when not knock limited. Based on the observed pressure traces and AHRR in Figure 9, it is postulated that the combustion process occurring in the developed operating strategy is primarily a lean pre-mixed reaction propagation regime: whether that is a fully propagating flame, flamelets, or a successively cascading autoignition zone driven process is unknown at this time.

What is known is that the $\phi_{premixed}$ at the higher loads in this work are conducive to flame propagation with methanol, with laminar flame speeds [37, 38] like that of methane [39] at the $\phi_{premixed}$ in this work. Moreover, with the early DI injection timings and long mixing times in addition to the higher trapped residuals the local equivalence ratio within the methanol entrained DI fuel spray would approach unity, potentially promoting local premixed turbulent flame propagation processes.

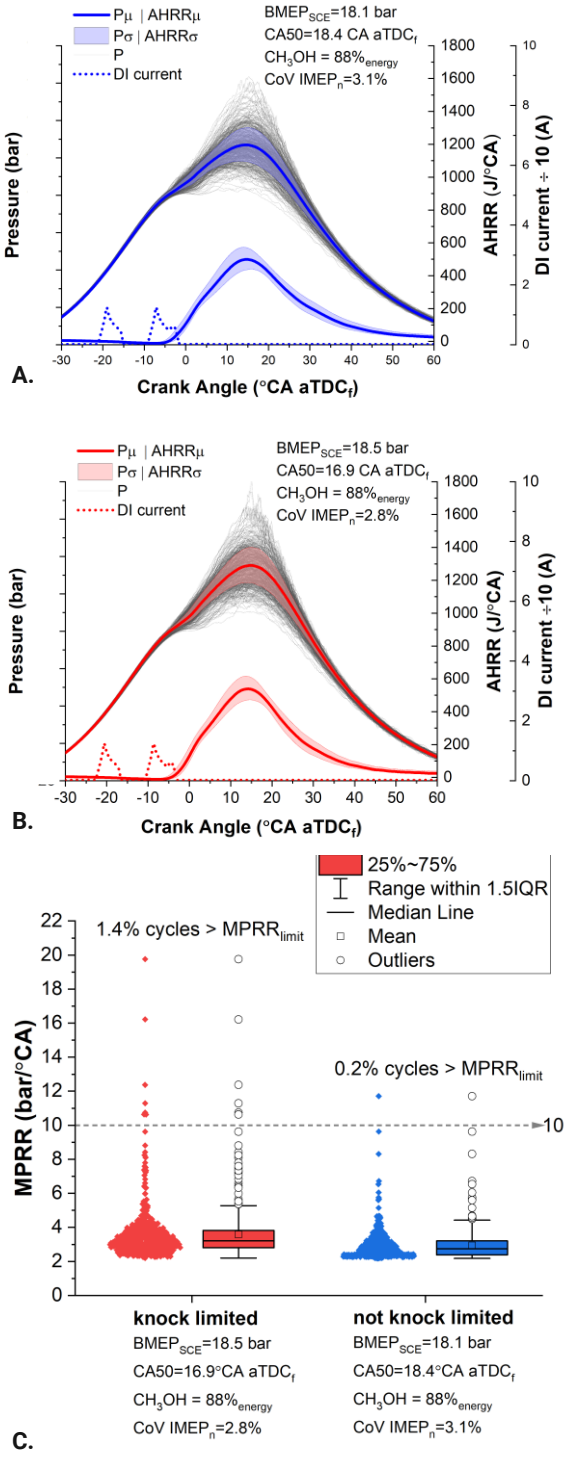

Figure 9. A. cyclic variation before the knock limit; B. knock-limited phasing and associated cyclic variation: grey lines are individual cycles, shaded region is 1 standard deviation of the mean, and solid lines are mean values, and dashed lines are direct injection current profile; C. MPRR of the data in figures A and B, highlighting the knock limit imposed of this study as less than 1% of the cycles over 10 bar/CA.

3.2.2 B100 methanol dual fuel controllability

The ULSD DI fuel was replaced with B100 to enable potential of a 100% renewably fueled engine (i.e., using B100 with renewable methanol). The results in Figure 10 indicate a similar combustion regime evolution with respect to load as seen with ULSD in Figure 6, demonstrating that high load operation (>15 bar BEMP) and high methanol substitution rates (>75%) with B100 as the DI fuel are possible.

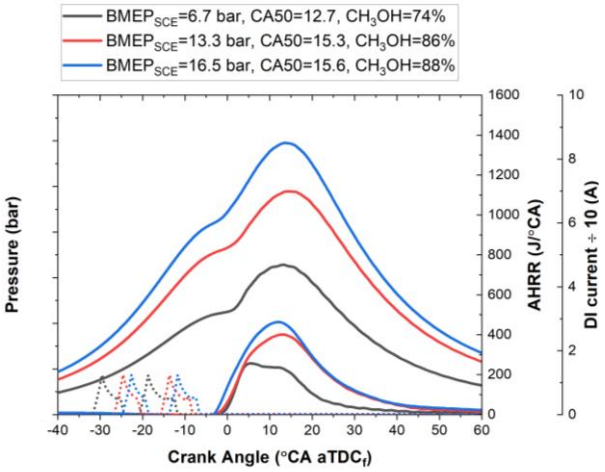

Figure 10. Mean values of indicated cylinder pressure, AHRR, and direct injection current commands for B100 as the DI fuel with high methanol substation levels in a load sweep.

3.3 Operational performance and emissions with ULSD and B100 as the DI fuel

The performance and emissions of the load sweeps of Figure 6 and Figure 10 are presented in Figure 11 and Figure 12 respectively. Figure 11 clearly shows that the ULSD-normalized BSFC and performance with B100 as the DI fuel can match that of ULSD. Also seen is that the MPRR and coefficient of variation of $IMEP_n$ are low across the load range with each DI fuel, below 10 bar/°CA and less than 5% respectively (except the lightest load with ULSD which just exceed 5% coefficient of variation (COV) of $IMEP_n$). Interestingly, Figure 11 depicts that the mass fraction burned (MFB) 5-50 (5% to 50%) combustion duration with B100 pilot fuel can be faster than with ULSD, especially at the higher loads, where the MPRR is thus correspondingly slightly higher. Note markers in both Figure 11 and Figure 12 are shaded by methanol percentage of the total fuel energy, and the CA50 of the associated DI fuels is also labeled. The shading and labels denote that between the two fuel there is little variation in the methanol percentages or the combustion phasing in the presented data.

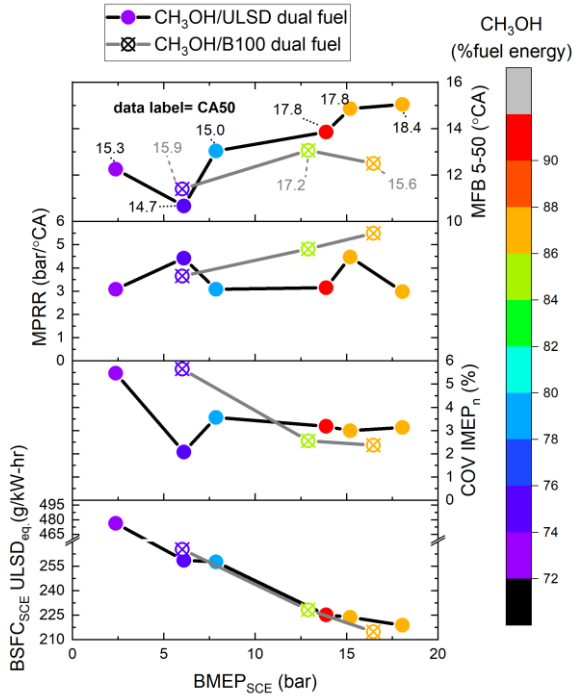

Figure 11. Trends in normalized BSFC (bottom), COV of $IMEP_n$ (second from bottom), Maximum pressure rise rate (second from top) and 5-50 % mass fraction burned (top) shown with respect to BMEP on the SCE ($BMEP_{SCE}$), marker color indicates the methanol substitution level by percent of total fuel energy.

To determine if there were any emissions differences between the DI fuel strategies key emissions are plotted in Figure 12. Generally, Figure 12 shows that both fuels exhibit extremely low FSN, with B100 being near the detection limit of the AVL 416S smoke meter used in this study. Interestingly, at matched CA50 combustion phasing there is no major emissions difference between B100 and ULSD. There is a slight increase in exhaust temperature with B100, suggesting increased in-cylinder temperatures, a trend that is possibly supported by a very slight increase in combustion efficiency at this matched condition (less than 1%). However, the most interesting observation is the oxides of nitrogen (NO_X) neutrality between B100 and ULSD at matched combustion phasing at similar loads, as this is not the same relation that occurs with B100 MCCI (Figure 14). Note that at the highest loads in Figure 12 the CA50 of the B100 DI fuel data is 2 to 3 crank angles advanced compared to the ULSD DI fuel data. Accordingly, the combustion phasing advance with B100 at this load increases NO_X emissions and the $BSFC_{SCE}$ on a ULSD fuel energy equlavent basis (ULSDeq.) fuel consumption is slightly lower and the MPRR is slightly higher (Figure 11) with B100 at this load.

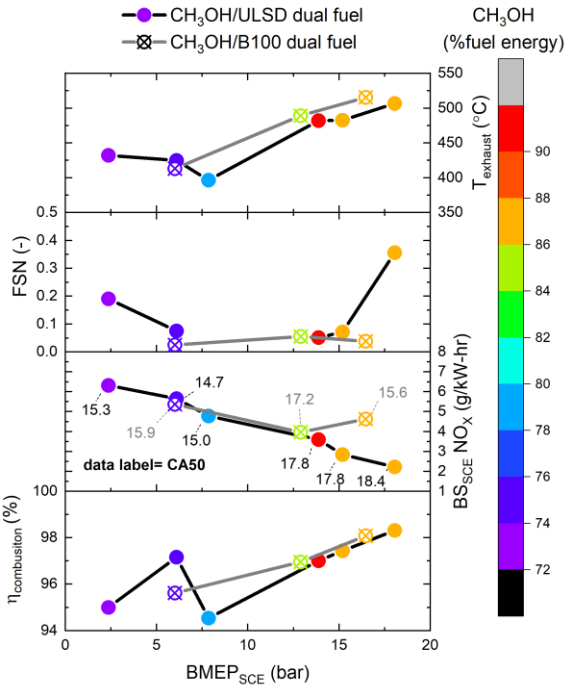

Figure 12. Trends in combustion efficiency (bottom), BS_{SCE} NO_X (second from bottom), FSN (second from top), and exhaust temperature (top) are shown with respect to $BMEP_{SCE}$. Marker color indicates the methanol substitution level by percent of total fuel energy.

In MCCI, elevated NO_X with B100 have been shown to be an artifact of increased local in-cylinder temperature at the flame front in diffusion flames due to increased local oxygen availability [40]. Although this is the driving force for NO_X emissions in diffusion combustion processes, the current dual fuel results highlight that B100 can be used in place of ULSD with minimal to no NO_X penalty. These NO_X neutral results with matched combustion phasing highlight that when the combustion mode with B100 is not intrinsically coupled to the spray a NO_X penalty with B100 does not occur. Note that the combustion rate differences and elevated exhaust temperature and combustion efficiency with B100 could be artifacts of physical process and mixing differences as documented by others [41], but the overall result observed is that there are no significant thermal increases at the flame front with B100 in methanol dual fuel combustion.

3.4 Emissions observations between ULSD and B100 methanol dual fuel and MCCI

The previous subsection highlighted that at matched condition there are no significant

emissions differences between B100 and ULSD in methanol dual fuel operation. This section explores additional effects of B100 in both dual fuel and MCCI combustion modes.

Figure 12 indicated that B100 as the DI fuel in methanol dual fuel did not exhibit significantly improved combustion efficiency and no significant change in NO_X emissions were measured as long as CA50 and operating conditions were the same. However, what was not indicated in Figure 12 was that B100 relative to ULSD as the DI fuel did enable an expanded operational window. Specifically, B100 as the DI fuel enabled richer $\phi_{premixed}$ operation. The source of this is thought to be enabled from the increased cetane number of B100 relative to ULSD, an effect that counteracts the reduced compression temperatures that result when increasing $\phi_{premixed}$ (Figure 5). Thus, the increased reactivity of B100 is thought to enable successful pilot fuel ignition at the richer $\phi_{premixed}$ conditions, expanding the operation window.

Although the operational window expands with B100, the richer $\phi_{premixed}$ reduces dilution, and thus increases in-cylinder temperatures and NO_X emissions. This direct $\phi_{premixed}$-NO_X relation with B100 is observed at approximately 12.5 bar BMEP operation in the data of Figure 13, where markers are shaded by $\phi_{premixed}$, the richer $\phi_{premixed}$ conditions also correspond to the increased brake specific NOx on the SCE ($BS_{SCE}NO_x$) emissions.

Figure 13, also depicts that combustion efficiency increases with both increased $\phi_{premixed}$ and $BS_{SCE}NO_x$ emissions. This tradeoff in NO_X and combustion efficiency is coupled to increase in-cylinder temperatures promoting methanol oxidization. The highest combustion efficiencies in Figure 13 corresponded to a methanol slip of less than 0.5%, (methanol sip is defined as the mass of methanol in the exhaust relative to the mass of methanol supplied to the engine).

These results indicate that B100 as the pilot fuel can achieve $BS_{SCE}NO_x$ neutrality with ULSD, but it is also able to operate at a broader range of conditions, which is primarily attributed to the cetane number increase of B100 relative to ULSD. Since ULSD was not able to operate at $\phi_{premixed}$ as rich as B100, a direct comparison between the fuels at this condition can not be made. However, what can be compared is the performance of B100 relative to ULSD in both methanol dual fuel and MCCI.

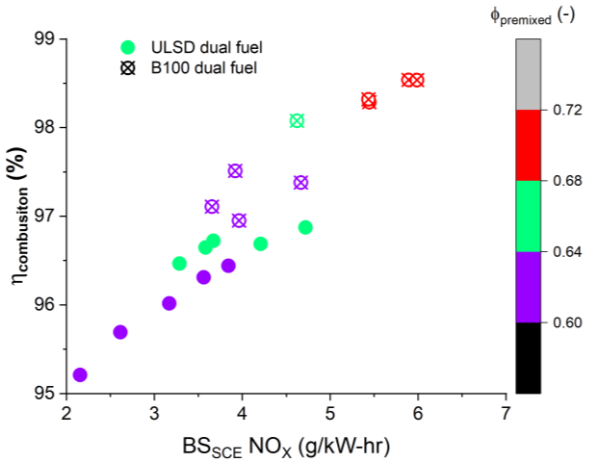

Figure 13. combustion efficiency plotted as a function of BE_{SCE} NO_X for ULSD (solid) and B100 (open x) markers at approximately 12.5 bar $BMEP_{SCE}$, markers are shaded by $\phi_{premixed}$.

The results of Figure 12 and Figure 13 highlight that in dual fuel operation when the operating conditions are similar between ULSD and B100, the NO_X emissions are also similar, a relation that is not ubiquitous across combustion regimes. For example, the difference in NO_X emissions with B100 for MCCI and dual fuel are depicted in Figure 14, which plots the ULSD-normalized BSFC as a function of $BS_{SCE}NO_x$ at approximately 12.5 bar $BMEP_{SCE}$. Markers in Figure 14 are shaded by CA50 for each combustion and fueling strategy, enabling a direct comparison of combustion phasing and NO_X. Data shows that for a given CA50, the $BS_{SCE}NO_x$ with B100 vs ULSD is approximately equal in dual-fuel operation, but in MCCI operation B100 fueling increases $BS_{SCE}NO_x$ by several g/kW-hr. Therefore, to operate at a NO_X neutral state with B100 in MCCI, combustion phasing must be retarded, and fuel consumption accordingly increases.

However, in dual fuel operation NO_X can be neutral between ULSD and B100, and no combustion phasing retard is needed for NO_X control. Moreover, Figure 14 also depicts that relative to MCCI, at a given combustion phasing, methanol dual fuel reduces NO_X by roughly 50%, with no change in ULSD-normalized BSFC fuel consumption, a significant observation on its own.

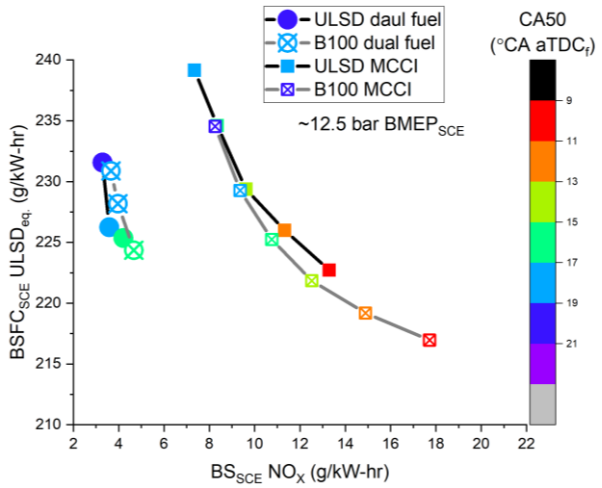

Figure 14. ULSD normalized SCE BSFC as a function of SCE BSNO$_x$ for B100 methanol dual fuel, ULSD methanol dual fuel, and ULSD MCCI at approximately 12.5 bar BMEP.

To better quantity the BS$_{SCE}$NO$_x$ emission of B100 the absolute increase in NO$_x$ with B100 relative to ULSD as the DI fuel in each combustion strategy was quantified using Equation 6, where $BS_{SCE}NO_{x,B100,CA50i}$ and $BS_{SCE}NO_{x,ULSD,CA50i}$ are the $BS_{SCE}NO_x$ for the respective fuels and combustion phasing. Thus, the difference is on a CA50 specific basis meaning that for a given CA50 what the increase in is absolute $BS_{SCE}NO_{x,}$.

$$\Delta NO_{x,B100} = BS_{SCE}NO_{x,B100,CA50i} - BS_{SCE}NO_{x,ULSD,CA50i} \quad (6)$$

The $\Delta NO_{x,B100}$ results of the data in Figure 14 are presented in Figure 15. The data shows that using B100, as the DI fuel in MCCI increases NO$_x$ by roughly 2 g/kW-hr, but in dual fuel operation NO$_X$ is effectively neutral between the DI fuels. Note, if the richer $\phi_{premixed}$ B100 data (red data in Figure 13) would have been compared to the leaner $\phi_{premixed}$ ULSD data than the $\Delta NO_{x,B100}$ with dual fuel would be approximately equal to that of B100 in MCCI, 2 g/kW-hr. Despite this, the absolute NO$_X$ in g/kW-hr, even with the richer $\phi_{premixed}$ B100 dual fuel, is at least 2 g/kW-hr lower than the lowest NOx ULSD (4 g/kW-hr with B100) in MCCI, where the MCCI data is also lower efficiency, highlighting the high efficiency with NO$_X$ reduction potential of the fuel fuel strategy.

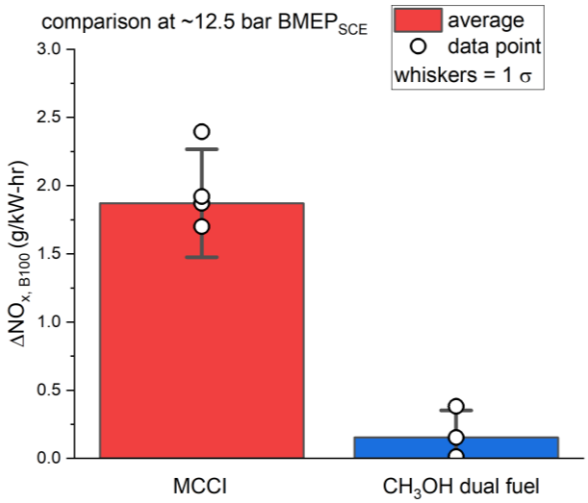

Figure 15. Bars indicating the mean $\Delta NO_{x,B100} = BS_{SCE}$ at approximately 12.5 bar BMEP for MCCI (red) and dual fuel (blue), whiskers represent one standard deviation, open circles depicting each data point used in determination of the average.

Interestingly, not only is the absolute magnitude of the NO$_X$ different but the composition of species fractions encompassing the NO$_X$ also differs between dual fuel and MCCI. In dual fuel methanol operation, most of the NO$_X$ emissions, regardless of the DI fuel, were found to be primarily NO$_2$, an unusual occurrence with conventional MCCI or SI. To quantify this observation the ratio of the NO$_2$ to total NO$_X$ was calculated, using Equation 7.

$$NO_{x,ratio} = 100 * \left(\frac{[NO_2]}{[NO_2] + [NO]}\right) \quad (7)$$

The corresponding $NO_{x,ratio}$ as a function of NO$_X$ are plotted in Figure 16, where the markers are colored as a function of engine load. A surprising result is that regardless of the DI fuel being B100 or ULSD, the methanol dual fuel trends in $NO_{x,ratio}$ are opposite those of MCCI. That is, the dual-fuel combustion strategy has the lowest measured $NO_{x,ratio}$ at the lowest operating loads, and MCCI has the highest measured $NO_{x,ratio}$ at its lightest loads. Note, despite the trends being opposite with respect to load, the absolute value of the $NO_{x,ratio}$ (and BS$_{SCE}$NO$_X$), converge at the lowest loads. It was observed in Figure 6 and Figure 10, that the AHRR of the dual fuel strategy at lighter loads was bimodal looking, with an MCCI like premixed burn and diffusion portion of the AHRR. This similarity in AHRR suggest similar combustion processes and thus at the light load conditions the similarity in $NO_{x,ratio}$ is logical.

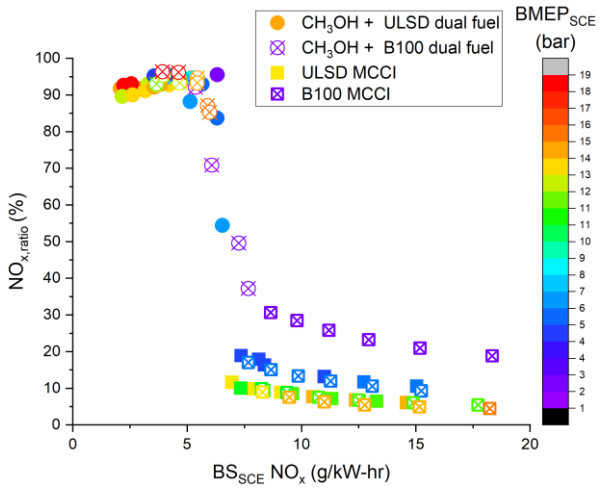

Figure 16. $NO_{x,ratio}$ plotted as a function of $BS_{SCE}NO_x$ for ULSD methanol dual fuel (closed circles), B100 methanol dual fuel (open crossed circles), ULSD MCCI (solid squares), and B100 MCCI (open cross marked squares). Markers are colored by $BMEP_{SCE}$.

However, at the higher loads the AHRR process evolves to a more homogeneously premixed propagating reaction behavior, e.g. SI-like combustion. What is peculiar is that under these conditions the total NO_X emission reduced but the $NO_{x,ratio}$ increases. Higher $NO_{x,ratio}$ in methanol dual fuel operation have been shown [42, 43], where the reaction of $NO+HO_2 \leftrightarrow NO_2 + OH$ were suspected to be a reaction pathway for the exceptionally high NO_2 emissions and associated $NO_{x,ratio}$. The production of HO_2 was shown to be exceptionally high with methanol dual fuel engines so the pathway to NO_2 was suggested to be more favorable. Interestingly, work in methanol spark ignition engines has also shown high NO_2 emissions, concentrations about 5 times those of gasoline or 3 times those of ethanol, but still peak $NO_{x,ratio}$ of that work was around 40% which occurred only under slightly rich conditions [44], under stoichiometric and lean conditions that work showed the $NO_{x,ratio}$ approached zero.

The $NO+HO_2 \leftrightarrow NO_2 + OH$ reaction pathways could be more prevalent in dual-fuel methanol engines than SI engines, suggesting an interplay of the DI fuel as a HO_2 source. Once formed, the associated sensitivity and activation thresholds with methanol may be lower than other traditional dual fuel approaches. To understand these pathway differences and sources, a detailed investigation is needed, which is beyond the scope of the present study. However, what can be gleaned from this work is that with B100-methanol dual fuel, the pathways are likely similar to those of ULSD dual fuel. That is, the $\Delta NO_{x,B100}$ associated with B100 is not a factor in affecting the $NO_{x,ratio}$, suggesting that methanol is the dominant factor in the $NO_{x,ratio}$ observed.

4 CONCLUSIONS

Results highlighted that premixed methanol ignited with direct injected ULSD or B100 could be operated with at least 75% methanol by energy from low to high loads while being within reasonable operational constraints (shown in Table 4). High loads—up to 19 bar BMEP in the SCE—were operated, with methanol substitution between 88–90% by energy. At low loads, down to 0.9 bar BMEP in the SCE, high methanol substitution rates of approximately 75% were also observed to be possible. Throughout the dual fuel operation, MPRR below 10 bar/°CA, combustion efficiency over 90%—even at 0.9 bar BMEP—and a COV of $IMEP_g$ of approximately 5% were maintained (note gross indicating mean effective pressure ($IMEP_g$) was used at only the lowest loads because of the low absolute $IMEP_n$).

The wide load operating range was found to be possible through reduced intake airflow and thus increased ϕ_{global} compared to MCCI operation at similar loads. Despite the reduced airflow, the FSN of the dual fuel approach was very low, with methanol and either ULSD or B100 dual fuel, with B100 exhibiting FSN levels approaching the detection limits of the AVL 415S smoke meter.

Throughout the load space, the BSFC normalized to ULSD on an energy basis was found to be the same if not better than MCCI at the same combustion phasing. That is, the ULSD-normalized BSFC with methanol dual fuel was equal to or better than MCCI for a given combustion phasing. Moreover, the dual fuel approach offered at least a 50% decrease in NO_x compared to the minimum NO_x for MCCI, conditions that for MCCI also increased BSFC. Thus, the dual fuel approach was found to offer even further improved BSFC if a low engine out NO_x calibration for MCCI was used.

Interestingly, in the dual fuel strategy, B100 was found to not increase NO_X compared to ULSD if the operating conditions were matched. B100 was also found to offer expanded operating window relative to ULSD, an attributed of cetane number of B100. At the richest $\phi_{premixed}$ with B100, nearly 99% combustion efficiency with 89% methanol by energy could be achieved.

Regardless of the pilot fuel, most of the NO_x emissions in dual fuel were found to be NO_2, approximately 90% by concentration. Moreover, the ratio of NO_2 to total NO_x was higher at higher loads. Further work is needed to elucidate the exact

chemical pathways for this, but the observations herein document the findings.

5 DEFINITIONS, ACRONYMS, ABBREVIATIONS

5-50: 5% to 50% mass fraction burned

°CA: degrees crank angle

$\phi_{premixed}$: premixed equivalence ratio

aTDC$_f$: after top dead center firing

B100: biodiesel

BMEP: brake mean effective pressure

BMEP$_{SCE}$: BMEP on the SCE

BSFC: brake specific fuel consumption

BS$_{SCE}$NO$_x$: brake specific NOx on the SCE

CA50: 50% mass fraction burned

COV: coefficient of variation

DI: direct injection

FSN: filter smoke number

HoV: enthalpy of vaporization

IMEP$_n$: net indicating mean effective pressure

MCCI: mixing-controlled compression ignition

MFB: mass fraction burned

MPRR: maximum pressure rise rate

NO$_X$: oxides of nitrogen

PFI: port fuel injection

rpm: revolution per minute

SCE: single cylinder engine

SOI: start of injection

TDC: top dead center

ULSD: ultra-low sulfur diesel

ULSDeq: ULSD fuel energy equlavent basis

6 ACKNOWLEDGMENTS

This work was funded under the cooperative research and development agreement CRADA NFE-22-09265 funded by the United States Department of Energy Vehicle Technologies office, United states Department of Transportation Maritime Administration, and with cost share and engineering support from Caterpillar.

7 REFERENCES AND BIBLIOGRAPHY

[1] Wissner, N., Healy, S., Cames, M. and Sutter, J., 2023. Methanol as a marine fuel. Naturschutzbund Deutschland: Stuttgart, Germany.

[2] Ammar, N.R., 2023. Methanol as a Marine Fuel for Greener Shipping: Case Study Tanker Vessel. *Journal of Ship Production and Design*, pp.1-11.

[3] Shi, J., Zhu, Y., Feng, Y., Yang, J. and Xia, C., 2023. A prompt decarbonization pathway for shipping: green hydrogen, ammonia, and methanol production and utilization in marine engines. *Atmosphere*, *14*(3), p.584.

[4] Svanberg, M., Ellis, J., Lundgren, J. and Landälv, I., 2018. Renewable methanol as a fuel for the shipping industry. *Renewable and Sustainable Energy Reviews*, *94*, pp.1217-1228.

[5] Kass, M.D., Sluder, C.S. and Kaul, B.C., 2021. *Spill behavior, detection, and mitigation for emerging nontraditional marine fuels* (No. DTMA91X20A65). United States. Department of Transportation. Maritime Administration.

[6] MARINE METHANOL Future-Proof Shipping Fuel, Methanol Institute, https://www.methanol.org/wp-content/uploads/2023/05/Marine_Methanol_Report_Methanol_Institute_May_2023.pdf

[7] Pan, W., Yao, C., Han, G., Wei, H. and Wang, Q., 2015. The impact of intake air temperature on performance and exhaust emissions of a diesel methanol dual fuel engine. Fuel, 162, pp.101-110.

[8] Wei, H., Yao, C., Pan, W., Han, G., Dou, Z., Wu, T., Liu, M., Wang, B., Gao, J., Chen, C. and Shi, J., 2017. Experimental investigations of the effects of pilot injection on combustion and gaseous emission characteristics of diesel/methanol dual fuel engine. Fuel, 188, pp.427-441.

[9] Xu, C., Zhuang, Y., Qian, Y. and Cho, H., 2022. Effect on the performance and emissions of methanol/diesel dual-fuel engine with different methanol injection positions. *Fuel*, *307*, p.121868.

[10] Dierickx, J., Verbiest, J., Janvier, T., Peeters, J., Sileghem, L. and Verhelst, S., 2021. Retrofitting a high-speed marine engine to dual-fuel methanol-diesel operation: A comparison of multiple and single point methanol port injection. *Fuel Communications*, *7*, p.100010.

[11] Karvounis, P., Theotokatos, G., Patil, C., Xiang, L. and Ding, Y., 2025. Parametric investigation of diesel–methanol dual fuel marine engines with port and direct injection. *Fuel*, *381*, p.133441.

[12] Geng, P., Yao, C., Wei, L., Liu, J., Wang, Q., Pan, W. and Wang, J., 2014. Reduction of PM emissions from a heavy-duty diesel engine with diesel/methanol dual fuel. *Fuel*, *123*, pp.1-11.

[13] Svanberg, M., Ellis, J., Lundgren, J. and Landälv, I., 2018. Renewable methanol as a fuel for the shipping industry. *Renewable and Sustainable Energy Reviews*, *94*, pp.1217-1228.

[14] Nemmour, A., Inayat, A., Janajreh, I. and Ghenai, C., 2023. Green hydrogen-based E-fuels (E-methane, E-methanol, E-ammonia) to support clean energy transition: A literature review. International Journal of Hydrogen Energy, 48(75), pp.29011-29033.

[15] Bos, M.J., Kersten, S.R. and Brilman, D.W.F., 2020. Wind power to methanol: Renewable methanol production using electricity, electrolysis of water and CO2 air capture. *Applied energy*, *264*, p.114672.

[16] Olah, G.A., 2013. Towards oil independence through renewable methanol chemistry. *Angewandte Chemie International Edition*, *52*(1).

[17] Rivarolo, M., Bellotti, D., Magistri, L. and Massardo, A.F., 2016. Feasibility study of methanol production from different renewable sources and thermo-economic analysis. *International Journal of Hydrogen Energy*, *41*(4), pp.2105-2116.

[18] Roode-Gutzmer, Q.I., Kaiser, D. and Bertau, M., 2019. Renewable methanol synthesis. *ChemBioEng Reviews*, *6*(6), pp.209-236.

[19] Methanol Institute https://www.methanol.org/renewable/

[20] Pinto, A.C., Guarieiro, L.L., Rezende, M.J., Ribeiro, N.M., Torres, E.A., Lopes, W.A., Pereira, P.A.D.P. and Andrade, J.B.D., 2005. Biodiesel: an overview. *Journal of the Brazilian Chemical Society*, *16*, pp.1313-1330.

[21] Kass, M.D., Abdullah, Z., Biddy, M.J., Drennan, C., Haq, Z., Hawkins, T., Jones, S., Holliday, J., Longman, D.E., Menter, S. and Newes, E., 2018. *Understanding the opportunities of biofuels for marine shipping* (No. ORNL/TM-2018/1080). Oak Ridge National Lab. (ORNL), Oak Ridge, TN (United States).

[22] ISO 8217:2017 Petroleum products — Fuels (class F) — Specifications of marine fuels, 2017, https://www.iso.org/standard/64247.html

[23] Products from petroleum, synthetic and renewable sources — Fuels (class F) — Specifications of marine fuels, 2024, https://www.iso.org/standard/80579.html

[24] CIMAC Guideline Marine-fuels containing FAME; A guideline for shipowners & operators, 2024, https://www.cimac.com/cms/upload/workinggroups/WG7/CIMAC_Guideline_Marine-fuels_containing_FAME_04-2024.pdf

[25] Kowalewicz, A., 1993. Methanol as a fuel for spark ignition engines: a review and analysis. *Proceedings of the Institution of Mechanical Engineers, Part D: Journal of Automobile Engineering*, *207*(1), pp.43-52.

[26] Brinkman, N., Halsall, R., Jorgensen, S.W. and Kirwan, J.E., 1994. The Development of Improved Fuel Specifications for Methanol (M85) and Ethanol (E d 85). *SAE transactions*, pp.361-374.

[27] Verhelst, S., Turner, J.W., Sileghem, L. and Vancoillie, J., 2019. Methanol as a fuel for internal combustion engines. *Progress in Energy and Combustion Science*, *70*, pp.43-88.

[28] Li, Y., Gong, J., Deng, Y., Yuan, W., Fu, J. and Zhang, B., 2017. Experimental comparative study on combustion, performance and emissions characteristics of methanol, ethanol and butanol in a spark ignition engine. *Applied Thermal Engineering*, *115*, pp.53-63.

[29] Wouters, C., Burkardt, P., Steeger, F., Fleischmann, M. and Pischinger, S., 2023. Comprehensive assessment of methanol as an alternative fuel for spark-ignition engines. *Fuel*, *340*, p.127627.

[30] Vancoillie, J., Demuynck, J., Sileghem, L., Van De Ginste, M., Verhelst, S., Brabant, L.V.H.L. and Van Hoorebeke, L., 2013. The potential of methanol as a fuel for flex-fuel and dedicated spark-ignition engines. *Applied Energy*, *102*, pp.140-149.

[31] Matsumoto, S., Klose, C., Schneider, J., Nakane, N., Ueda, D. and Kondo, S., 2013. *4 th Generation Diesel Common Rail System: Realizing Ideal Structure Function for Diesel Engine* (No. 2013-01-1590). SAE Technical Paper.

[32] Heywood, J.B., 1988. Internal combustion engine fundamentals.

[33] Eyidogan, M., Ozsezen, A.N., Canakci, M. and Turkcan, A., 2010. Impact of alcohol–gasoline fuel blends on the performance and combustion characteristics of an SI engine. *Fuel*, *89*(10), pp.2713-2720.

[34] Johnston, T., Zeman, J. and Dempsey, A., 2024. Mixing-controlled compression ignition of ethanol using exhaust rebreathe at a low-load operating condition—Single cylinder experiments in a heavy-duty diesel engine. *International Journal of Engine Research*, p.14680874241293823.

[35] Smith, J.M., Van Ness, and Abbott, Introduction to chemical engineering thermodynamics fifth edition, 1996.

[36] Ma, B., Yao, A., Yao, C., Chen, C., Qu, G., Wang, W. and Ai, Y., 2021. Multiple combustion modes existing in the engine operating in diesel methanol dual fuel. *Energy*, *234*, p.121285.

[37] Gülder, Ö.L., 1982, January. Laminar burning velocities of methanol, ethanol and isooctane-air mixtures. In *Symposium (international) on combustion* (Vol. 19, No. 1, pp. 275-281). Elsevier.

[38] Veloo, P.S., Wang, Y.L., Egolfopoulos, F.N. and Westbrook, C.K., 2010. A comparative experimental and computational study of methanol, ethanol, and n-butanol flames. *Combustion and Flame*, *157*(10), pp.1989-2004.

[39] Egolfopoulos, F.N., Cho, P. and Law, C.K., 1989. Laminar flame speeds of methane-air mixtures under reduced and elevated pressures. *Combustion and flame*, *76*(3-4), pp.375-391.

[40] Mueller, C.J., Boehman, A.L. and Martin, G.C., 2009. An experimental investigation of the origin of increased NOx emissions when fueling a heavy-duty compression-ignition engine with soy biodiesel. *SAE International Journal of Fuels and Lubricants*, *2*(1), pp.789-816.

[41] Szybist, J.P., Song, J., Alam, M. and Boehman, A.L., 2007. Biodiesel combustion, emissions and emission control. *Fuel processing technology*, *88*(7), pp.679-691.

[42] Huang, Q., Yang, R., Liu, J., Xie, T. and Liu, J., 2024. Investigation of the mechanism behind the surge in nitrogen dioxide emissions in engines transitioning from pure diesel operation to methanol/diesel dual-fuel operation. *Fuel Processing Technology*, *264*, p.108131.

[43] Lu, H., Yao, A., Yao, C., Chen, C. and Wang, B., 2019. An investigation on the characteristics of and influence factors for NO2 formation in diesel/methanol dual fuel engine. *Fuel*, *235*, pp.617-626.

[44] Ito, K. and Fujita, O., 1985, January. The effects of NO2 on catalytic oxidation of unburned species from a methanol fueled spark ignition engine. In *Symposium (International) on Combustion* (Vol. 20, No. 1, pp. 53-59). Elsevier.

8 CONTACT

Derek Splitter splitterda@ornl.gov